Oil Spill Drift Prediction Enhanced by Correcting Numerically Forecasted Sea Surface Dynamic Fields With Adversarial Temporal Convolutional Networks

Peng Ren, *Senior Member, IEEE*, Qilin Jia, Qing Xu, Yongqing Li, Fan Bi, Jiangling Xu, and Song Gao

***Abstract*— Timely and accurate representation of sea surface dynamic fields is crucial for oil spill drift prediction. Numerically forecasted sea surface dynamic fields are available in a timely manner, but their accuracy is limited. Conversely, reanalysis sea surface dynamic fields offer superior accuracy but suffer from time delays. To enhance the performance of oil spill drift prediction, we propose a deep-learning-based approach to correcting numerically forecasted sea surface dynamic fields, aligning them more closely with reanalysis sea surface dynamic fields. Our approach introduces an adversarial temporal convolutional network (ATCN) framework, consisting of a temporal convolutional network (TCN)-based corrector and a discriminator. The TCN can characterize sea surface dynamic field sequences both spatially and temporally. In this scenario, the corrector processes the numerically forecasted sea surface dynamic fields and outputs corrected sea surface dynamic fields that approximate the reanalysis sea surface dynamic fields. Adversarial training with the discriminator further refines the corrector. This approach enhances timely oil spill drift prediction using the corrected sea surface dynamic fields. We also provide a dataset of oil spill drifts from the Symphony and Sanchi accidents, including related sea surface dynamic field data and oil spill remote sensing data, establishing a baseline for evaluating oil spill drift prediction. Experiments on this dataset validate the ATCN framework's effectiveness in enhancing oil spill drift prediction.**

***Index Terms*— Adversarial temporal convolutional networks (ATCNs), oil spill drift prediction, sea surface dynamic fields.**

I. Introduction

THE impacts of oil spills on damaging marine ecosystems and economies have been widely recognized [1], [2], [3], [4], [5]. One important effort to quickly respond and mitigate these negative impacts is the timely and accurate prediction of oil spill drifts [1], [6], [7]. In this scenario, timely and accurate data representing sea surface dynamic fields, which drive oil spill drifts, play a crucial role [8].

Dynamic field data can be obtained through various methods, with two major families stemming from numerical forecast and reanalysis. The two families are complementary in terms of timeliness and accuracy. In addition, both require remote sensing for data refinement.

In this section, we begin by reviewing the research literature on numerically forecasted sea surface dynamic fields and reanalysis sea surface dynamic fields. We then compare them and discuss their complementarity. Following this, we review oil spill drift prediction and propose a deep learning-based approach to enhancing oil spill drift prediction. Finally, we summarize our novel contributions and give the organization of this article.

A. Review of Numerically Forecasted Sea Surface Dynamic Fields

Numerically forecasted sea surface dynamic fields are data generated by numerical models to depict forecasted future sea surface dynamic situations.

The global forecast system (GFS) by the National Centers for Environmental Prediction (NCEP) was among the first to provide numerically forecasted sea surface dynamic fields [9]. The European Centre for Medium-Range Weather Forecasts (ECMWF) established an integrated forecasting system, referenced in Roberts' 2018 climate study. In addition, the United States Navy developed the Navy Coupled Ocean Data Assimilation (NCODA), which contributed to the launch of the global ocean forecasting system (GOFS). These forecasting systems are indispensable, providing essential resources of numerically forecasted sea surface dynamic fields for both research and practical applications.

Numerically forecasted sea surface dynamic fields are generated by numerical models rooted in physical laws [10]. They can be obtained in a timely manner. However, their accuracy is limited. First, numerical models are formulated as physical equations that follow ocean dynamic laws but lack fine variability. Second, observational data, especially remote sensing data, can just be partially used to initialize numerical models for forecasting future dynamic fields. Despite efforts

Received 22 June 2024; revised 24 September 2024 and 30 December 2024; accepted 8 January 2025. Date of publication 13 January 2025; date of current version 7 February 2025. This work was supported in part by the National Natural Science Foundation of China under Project 42406216 and Project 61971444, in part by Shandong Provincial Natural Science Foundation under Project ZR2024QD031, and in part by Taishan Scholar Project. *(Corresponding author: Yongqing Li.)*

Peng Ren, Qilin Jia, and Qing Xu are with the College of Oceanography and Space Informatics, China University of Petroleum (East China), Qingdao 266580, China (e-mail: pengren@upc.edu.cn; qilinjia_upc@163.com; xuqing_upc@163.com).

Yongqing Li is with the School of Data Science, Qingdao University of Science and Technology, Qingdao 266061, China (e-mail: liyongqing@qust.edu.cn).

Fan Bi, Jiangling Xu, and Song Gao are with North China Sea Forecast and Hazard Mitigation Center, Ministry of Natural Resources, Qingdao 266061, China (e-mail: bifan@ncs.mnr.gov.cn; xujiangling@ncs.mnr.gov.cn; gaosong@ncs.mnr.gov.cn).

Digital Object Identifier 10.1109/TGRS.2025.3528631

to assimilate observational data, its capability to improve forecasted future dynamic fields is constrained.

B. Review of Reanalysis Sea Surface Dynamic Fields

Reanalysis sea surface dynamic fields are generated through reanalyzing numerically forecasted sea surface dynamic fields by referencing an extensive array of high-quality remote sensing and in situ historical observations [1], [5]. They are widely considered as accurate representations of sea surface dynamic fields.

The collaboration between NCEP and the National Center for Atmospheric Research (NCAR) resulted in the development of the Reanalysis-1 model [11], which comprehensively addresses complex conditions, including those in coastal regions [12]. This effort was further advanced by the Reanalysis-2 model, jointly proposed by NCEP and the Department of Energy (DOE) [13]. In addition, the ECMWF significantly contributed a series of reanalysis models, including ERA-40 [14], ERA-Interim [15], and ERA-5 [16]. These schemes provide reanalysis sea surface dynamic fields as accurate resources for various research and practical operations.

While reanalysis sea surface dynamic fields rely heavily on historical observations to maintain their high accuracy, they inevitably suffer from long time delays [17].

C. Comparison Between Numerically Forecasted and Reanalysis Data, and Their Complementarity

Numerically forecasted sea surface dynamic fields are generated by numerical models to depict future sea surface dynamic situations. They can provide timely data for driving oil spill drift prediction models. Conversely, reanalysis sea surface dynamic fields are historical data that represent past dynamic fields. They cannot be directly used for driving oil spill drift prediction models because of their latency.

On the other hand, the accuracy of numerically forecasted sea surface dynamic fields is limited because these fields are generated by solving fixed physical equations with observations as partial initializations. Conversely, reanalysis sea surface dynamic fields are much more accurate because they involve plenty of remote sensing and in situ historical observations for reanalyzing the numerically forecasted sea surface dynamic fields.

Accesses to numerically forecasted and reanalysis data related to sea surface dynamic fields on a global scale is primarily facilitated through institutions such as NCEP, NCAR, ECMWF, CMEMS, and HYCOM. The pros and cons of numerically forecasted sea surface dynamic fields and reanalysis sea surface dynamic fields are summarized in Table I. It is observed that they are complementary in terms of timeliness and accuracy. It is anticipated that data representation which takes advantages of both the timeliness of numerical forecast and the accuracy of reanalysis can be explored for oil spill drift prediction.

D. Review of Oil Spill Drift Prediction and Proposal for Its Enhancement

One representative method for oil spill drift prediction is the Lagrangian scheme [18], which considers oil spills as a collection of discrete particles and drives the oil spill particles using wind and current fields. The Stokes drift model is another typical method which takes more comprehensive dynamic fields into consideration. Although various oil spill drift prediction models have been developed, it is widely accepted that the drift of oil spills is predominantly influenced by sea surface dynamic forces [19] including winds, currents, etc.

Most existing methods for predicting oil spill drift trajectories heavily rely on numerically forecasted sea surface dynamic fields, sourced from operational forecasting systems. Liu et al. [20], [21], [22] demonstrated the feasibility of merging satellite imagery of oil spills with numerical models of ocean circulation for the purpose of capturing oil spill movements, especially in the Deepwater Horizon incident. The OILTRANS model [23] exemplified oil spill drift prediction in the Celtic Sea. Cheng et al. [24] applied an operational forecasting model to delineate the trajectory of oil spills from the Gannet Alpha platform. Jones et al. [25] analyzed the drift dynamics of various oil types in the North Sea. Röhrs et al. [26] used the OpenOil model to investigate drift processes. Brekke et al. [27] conducted a comparative study of oil spill drift prediction referencing remote sensing and in situ observations, underscoring the critical influence of wind and current on oil spill drift prediction. The numerical forecasting systems can provide timely representations of future sea surface dynamic fields to drive oil spill drift models. However, their accuracy tends to be limited as discussed in Sections I-A and I-C.

Numerous attempts using traditional techniques such as Kalman filtering and support vector machines have been made in improving forecasted sea surface dynamic fields [28], [29], [30], [31], [32], [33], [34], [35], [36]. These methods apply to a wide range and consider various environmental factors, geographical location, and model errors. Furthermore, there are forecast correction methods tailored for specific models and data sources, such as the Aladin model and the ECMWF numerical weather prediction model [32], [36], [37], [38]. In recent years, deep learning has significantly advanced remote sensing technology in both land and ocean observation [39], [40], [41], [42], [43], [44], [45], [46], [47], [48], [49], [50], [51], [52], [53], [54], [55]. More recently, utilization of various deep learning models for improving sea surface dynamic field forecasts has emerged as a remarkable trend. These deep learning methods encompass convolutional neural networks (CNNs), recurrent neural networks (RNNs), and long short-term memory (LSTM) networks, among others. Notably, advancements such as the adversarial ConvLSTM network [56] and the self-attention temporal convolutional network (TCN) [57], which are enhancements based on LSTM and TCN, respectively, have been applied to wind field correction, yielding effective outcomes. However, these methods have limitations in comprehensively characterizing both temporal and spatial variations.

Based on the above reviewed literature, we make three key observations. First, numerically forecasted sea surface dynamic fields and reanalysis sea surface dynamic fields can form data pairs that train deep learning models to correct the

TABLE I
TIMELINESS AND ACCURACY OF SEA SURFACE DYNAMIC FIELDS

Data	Agency	Update	Timeliness	Accuracy
Numerically forecasted sea surface dynamic fields	NCEP	+14 days	✓	✗
	HYCOM	+5 days		
Reanalysis sea surface dynamic fields	CMEMS	-7 days	✗	✓
	ECMWF	-5 days		

former, approximating them to the latter. Second, sea surface dynamic fields exhibit rich temporal and spatial information, highlighting the need for a new deep learning framework that comprehensively captures both temporal and spatial variations to correct numerically forecasted sea surface dynamic fields using their corresponding reanalysis data. Third, the corrected sea surface dynamic fields are expected to drive oil spill drift prediction models in a timely and accurate manner. In light of these observations, we propose to develop an adversarial TCN (ATCN) framework to correct numerically forecasted sea surface dynamic fields, aligning them more closely with reanalysis data, and use these corrected sea surface dynamic fields as driving forces for oil spill drift prediction.

E. Novel Contributions

The main novel contributions of this article are summarized as follows.

1) *ATCNs for Sea Surface Dynamic Field Correction:* A novel ATCN framework is introduced to effectively correct numerically forecasted sea surface dynamic fields by capturing spatial correlations and temporal variations (see Section II). It produces corrected sea surface dynamic fields that closely align with reanalysis data, enabling timely and accurate representation of sea surface dynamic fields.
2) *Oil Spill Drift Prediction Enhanced by the Corrected Sea Surface Dynamic Fields:* We propose using the corrected sea surface dynamic fields obtained through the ATCN framework as driving forces for oil spill drift prediction models (see Section III). This approach enhances the performance of oil spill drift prediction with superior prediction outcomes.
3) *Baseline Dataset for Evaluating Oil Spill Drift Prediction:* The effectiveness of the proposed oil spill drift prediction method is evaluated by comprehensive experiments on data related to the Sanchi and Symphony oil spill accidents. We release the dataset and code for public evaluations (see Section IV).

F. Article Organization

The structure of this article is outlined as follows: Section II introduces the ATCN framework, the training process of the ATCNs, and the sea surface dynamic field correction with the trained ATCNs. Section III presents a sea surface dynamic field correction-based oil spill drift prediction (SDFCP) strategy. Section IV presents the datasets, which include various sea surface dynamic field data and oil spill remote sensing data for the Symphony and Sanchi accidents. Section V presents the experimental results, which validate the correction performance of the ATCNs and validate the effectiveness of the SDFCP strategy. Finally, Section VI provides the concluding thoughts for this article.

II. ATCNs FOR SEA SURFACE DYNAMIC FIELD CORRECTION

In this section, we introduce ATCNs for correcting numerically forecasted sea surface dynamic fields. Section II-A introduces the overall ATCN framework, which consists of a corrector and a discriminator. Sections II-B and II-C introduce the architectures of the corrector and the discriminator, respectively. Section II-D introduces the loss functions for training the corrector and the discriminator. Section II-E introduces the proposed sea surface dynamic field correction approach.

A. Framework Overview

A dynamic field has two components in the u- and v-directions. In our work, the two components are processed separately in the same manner. Before Section V (i.e., the section of experimental evaluations), each component will be indiscriminately referred to as a dynamic field for the purpose of concise formulations. Let $\boldsymbol{F}_t^f$, $\boldsymbol{F}_t^r$, and $\boldsymbol{F}_t^c$ denote the numerically forecasted sea surface dynamic field, the reanalysis dynamic field, and the corrected dynamic field at time t, respectively.

Fig. 1 illustrates the proposed ATCN framework, which consists of a corrector and a discriminator. The corrector takes a sequence of numerically forecasted sea surface dynamic fields $\{\boldsymbol{F}_{t-T_1}^f, \ldots, \boldsymbol{F}_t^f, \ldots, \boldsymbol{F}_{t+T_2}^f\}$ as input, and produces a corrected sea surface dynamic field $\boldsymbol{F}_t^c$ for the numerically forecasted sea surface dynamic field $\boldsymbol{F}_t^f$ as output. The discriminator takes either $\{\boldsymbol{F}_t^c, \boldsymbol{F}_t^f\}$ pair or $\{\boldsymbol{F}_t^r, \boldsymbol{F}_t^f\}$ pair as input, and outputs a score reflecting the similarity between the two dynamic fields in one pair.

The corrector and the discriminator are trained in an adversarial manner until the corrector produces corrected sea surface dynamic fields which closely approximate the reanalysis sea surface dynamic fields. This adversarial training approach refines the corrector's ability, in favor of improving correction accuracy.

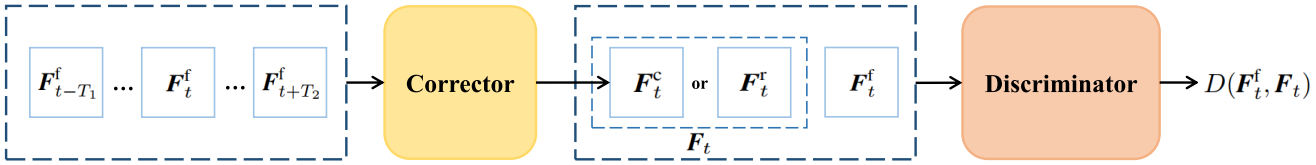

Fig. 1. Adversarial temporal convolutional networks.

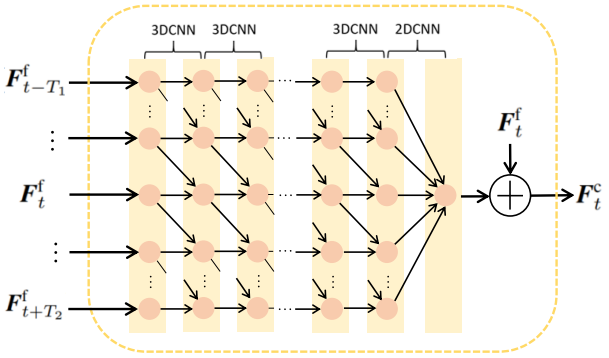

Fig. 2. Corrector.

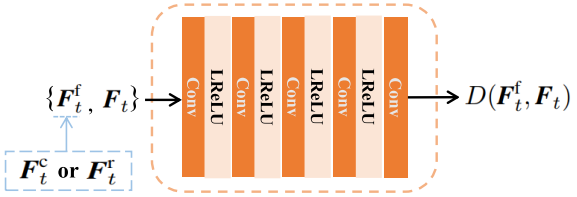

Fig. 3. Discriminator.

B. Corrector

As illustrated in Fig. 2, the corrector consists of L 3-D CNN (3DCNN) modules, one 2DCNN module, and a residual learning operation. The corrector takes a sequence of numerically forecasted sea surface dynamic fields $\{\boldsymbol{F}^{f}_{t-T_1}, \ldots, \boldsymbol{F}^{f}_{t}, \ldots, \boldsymbol{F}^{f}_{t+T_2}\}$ as input, and produces a corrected sea surface dynamic field $\boldsymbol{F}^{c}_{t}$ for the numerically forecasted sea surface dynamic field $\boldsymbol{F}^{f}_{t}$ as output. The 3DCNN modules operate causal convolutions. The sequence $\{\boldsymbol{H}^{l}_{t-T_1}, \ldots, \boldsymbol{H}^{l}_{t}, \ldots, \boldsymbol{H}^{l}_{t+T_2}\}$ are the output feature maps from the lth 3DCNN layer, where $1 \le l \le L$.

They are computed as follows:

$$\begin{aligned}&\{\boldsymbol{H}^{l}_{t-T_1}, \ldots, \boldsymbol{H}^{l}_{t}, \ldots, \boldsymbol{H}^{l}_{t+T_2}\}\\ &\quad = \text{3DCNN}\left(\boldsymbol{H}^{l-1}_{t-T_1}, \ldots, \boldsymbol{H}^{l-1}_{t}, \ldots, \boldsymbol{H}^{l-1}_{t+T_2}\right)\end{aligned} \tag{1}$$

where 3DCNN$(\cdot)$ denotes the operations performed by the 3DCNN module. The causal convolutions ensure that $\boldsymbol{H}^{l}_{t}$ depends only on the previous feature map sequence $\{\boldsymbol{H}^{l-1}_{t-T_1}, \ldots, \boldsymbol{H}^{l-1}_{t}\}$. The Lth 3DCNN module outputs $\{\boldsymbol{H}^{L}_{t-T_1}, \ldots, \boldsymbol{H}^{L}_{t}, \ldots, \boldsymbol{H}^{L}_{t+T_2}\}$. The output of the final 3DCNN module is the input to the 2DCNN module. Let 2DCNN$(\cdot)$ denote the operations performed by the 2DCNN module. As illustrated in Fig. 2, the corrector uses a residual learning strategy, which adds the numerically forecasted sea surface dynamic field $\boldsymbol{F}^{f}_{t}$ to the output of the 2DCNN. The corrected sea surface dynamic field $\boldsymbol{F}^{c}_{t}$ is given by

$$\boldsymbol{F}^{c}_{t} = \boldsymbol{F}^{f}_{t} + \text{2DCNN}\left(\boldsymbol{H}^{L}_{t-T_1}, \ldots, \boldsymbol{H}^{L}_{t}, \ldots, \boldsymbol{H}^{L}_{t+T_2}\right). \tag{2}$$

The TCN effectively extracts spatial and temporal features from the dynamic field sequence, rendering the corrected sea surface dynamic field $\boldsymbol{F}^{c}_{t}$ by considering comprehensive spatiotemporal variations.

C. Discriminator

As illustrated in Fig. 3, the discriminator consists of five convolutional layers, with LReLU activation functions following the first four layers. The discriminator takes $\{\boldsymbol{F}_t, \boldsymbol{F}^{f}_{t}\}$ as input, where $\boldsymbol{F}_t$ can be either $\boldsymbol{F}^{c}_{t}$ or $\boldsymbol{F}^{r}_{t}$. The output $D(\boldsymbol{F}_t, \boldsymbol{F}^{f}_{t})$ is a score representing the average value of the feature map generated by the discriminator's final convolutional layer, where $D(\cdot, \cdot)$ denotes the discriminator's operations. A big score of $D(\boldsymbol{F}_t, \boldsymbol{F}^{f}_{t})$ reflects that the $\boldsymbol{F}_t$ closely aligns with $\boldsymbol{F}^{r}_{t}$.

D. Training

Let L_{C_t} denote the loss function for training the corrector. It penalizes the difference between the corrected sea surface dynamic fields and the reanalysis sea surface dynamic fields and also penalizes the correct judgment of the discriminator. It is given by

$$L_{C_t} = \lambda_1 \left\|\boldsymbol{F}^{r}_{t} - \boldsymbol{F}^{c}_{t}\right\|_1 - D\left(\boldsymbol{F}^{c}_{t}, \boldsymbol{F}^{f}_{t}\right) \tag{3}$$

where λ_1 is a balancing parameter, $\|\boldsymbol{F}^{r}_{t} - \boldsymbol{F}^{c}_{t}\|_1$ is an ℓ_1-norm loss, and $-D(\boldsymbol{F}^{c}_{t}, \boldsymbol{F}^{f}_{t})$ is an adversarial loss. Minimizing (3) trains the corrector to align $\boldsymbol{F}^{c}_{t}$ closely with $\boldsymbol{F}^{r}_{t}$.

Let L_{D_t} denote the loss function for training the discriminator. Minimizing it aims to improve its ability to distinguish between the corrected sea surface dynamic fields and the reanalysis sea surface dynamic fields. It is given by

$$\begin{aligned}L_{D_t} = &\left[D\left(\boldsymbol{F}^{c}_{t}, \boldsymbol{F}^{f}_{t}\right) - D\left(\boldsymbol{F}^{r}_{t}, \boldsymbol{F}^{f}_{t}\right)\right]\\ &+ \lambda_2 \left[\left\|\nabla_{\tilde{\boldsymbol{F}}_t} D\left(\tilde{\boldsymbol{F}}_t, \boldsymbol{F}^{f}_{t}\right)\right\|_2 - 1\right]^2\end{aligned} \tag{4}$$

where λ_2 is a balancing parameter, $\tilde{\boldsymbol{F}}_t$ is a randomly sampled value between $\boldsymbol{F}^{c}_{t}$ and $\boldsymbol{F}^{r}_{t}$, the term $\left[D(\boldsymbol{F}^{f}_{t}, \boldsymbol{F}^{c}_{t}) - D(\boldsymbol{F}^{f}_{t}, \boldsymbol{F}^{r}_{t})\right]$ captures the adversarial loss, driving the discriminator to see $\boldsymbol{F}^{c}_{t}$ as fake and $\boldsymbol{F}^{r}_{t}$ as real, and the term $\left[\|\nabla_{\tilde{\boldsymbol{F}}_t} D(\tilde{\boldsymbol{F}}_t, \boldsymbol{F}^{f}_{t})\|_2 - 1\right]^2$ is the gradient penalty loss, aiming to keep gradient stability. Minimizing (4) trains the discriminator to distinguish $\boldsymbol{F}^{c}_{t}$ from $\boldsymbol{F}^{r}_{t}$.

E. Wind and Current Field Correction

In this section, we introduce the proposed sea surface dynamic field correction approach, using the ATCN framework.

The training process of the ATCNs is given in Algorithm 1. The training alternates between the corrector and the discriminator in an adversarial manner. This means they compete to improve their abilities. The corrector is trained to make better corrections. The discriminator is trained to better distinguish the fields. The training stops when the discriminator keeps giving constant scores, such that it cannot distinguish between the corrected sea surface dynamic fields and the reanalysis sea surface dynamic fields. At this point, both the corrector and the discriminator have reached their best performance where the corrector generates the most accurate corrected sea surface dynamic fields.

Algorithm 1 Training Process of the ATCNs

Input: The training dataset, comprising numerically forecasted sea surface dynamic fields and their corresponding reanalysis sea surface dynamic fields.

Output: The trained ATCNs parameters.

for each training epoch **do**

for each training data sample **do**

Input a sequence of numerically forecasted sea surface dynamic fields $\{\boldsymbol{F}^f_{t-T_1}, \ldots, \boldsymbol{F}^f_t, \ldots, \boldsymbol{F}^f_{t+T_2}\}$ and a reanalysis sea surface dynamic field $\boldsymbol{F}^r_t$.

Compute the corrected sea surface dynamic field $\boldsymbol{F}^c_t$ according to (2).

Train the discriminator: Update the parameters of the discriminator by minimizing L_{D_t} in (4).

Train the corrector: Update the parameters of the corrector by minimizing L_{C_t} in (3).

end for

end for

As described in Section I-C, the reanalysis wind fields and the analysis current fields are considered accurate. They are used as the ground-truth wind fields and current fields. Although the ATCNs need reanalysis wind fields and analysis current fields during training, they do not need these fields during practical operations. Therefore, the corrected sea surface dynamic fields are obtained without delay and they can enable timely and accurate oil spill drift prediction.

III. Oil Spill Drift Prediction Enhanced by the Corrected Sea Surface Dynamic Fields

In this section, we develop an SDFCP strategy. To this end, we commence by presenting a basic oil spill drift prediction strategy, as illustrated in Fig. 4, where the core is an oil spill drift numerical prediction model. The oil spill drift numerical prediction model is normally formulated subject to a Lagrangian scheme that considers oil spills as a collection of individual particles [19]. In this scenario, oil spill drift prediction is transformed into predicting the drift of a large number of oil spill particles. The oil spill drift numerical prediction model is mainly driven by two factors, sea surface wind fields and sea surface current fields [58], [59]. Therefore, the inputs of the model include oil spill positions extracted from remote sensing data, numerically forecasted wind fields, and numerically forecasted current fields, and the outputs are predicted oil spill particle positions.

As presented in Section II-A, a dynamic field has two components in the u- and v-directions, separately. For an oil spill particle, let w^u_t and w^v_t denote the sea surface wind field components at time t in the eastward and northward directions, respectively. Similarly, let c^u_t and c^v_t denote the sea surface current components in the eastward and northward directions, respectively.

Let u_p and v_p denote the eastward (u) and northward (v) drift speed components, respectively. They are given by

$$\begin{aligned} u_p &= \alpha_w w^u_t + \alpha_c c^u_t \\ v_p &= \alpha_w w^v_t + \alpha_c c^v_t \end{aligned} \tag{5}$$

where α_w and α_c denote the weighting factors for the wind speed and the current speed, respectively.

Let Δt denote the time increment for oil spill drift. Let Δx_p and Δy_p denote the eastward (u) and northward (v) components of drift displacement, respectively. The two displacement components over Δt are given by

$$\begin{aligned} \Delta x_p &= u_p \Delta t \\ \Delta y_p &= v_p \Delta t. \end{aligned} \tag{6}$$

Let R_n denote a random variable with a zero mean and a unit variance, μ denote a parameter for weighting the randomness in movement, E_r denote the rate of horizontal random motion, and θ denote a directional angle uniformly distributed over a circle. Let Δx_r and Δy_r denote the eastward (u) and northward (v) components of random movement displacement, respectively. They are given by

$$\begin{aligned} \Delta x_r &= R_n \sqrt{\mu E_r \Delta t} \cos\theta \\ \Delta y_r &= R_n \sqrt{\mu E_r \Delta t} \sin\theta. \end{aligned} \tag{7}$$

Let Δx and Δy denote the eastward (u) and northward (v) components of the total drift displacement, respectively. They are given by

$$\begin{aligned} \Delta x &= \Delta x_p + \Delta x_r \\ \Delta y &= \Delta y_p + \Delta y_r. \end{aligned} \tag{8}$$

Let (x_t, y_t) denote the geographical coordinates (i.e., longitude and latitude) of an oil spill particle at time t. Let γ denote the displacement that corresponds to one degree of latitude along the same meridian. The position $(x_{t+\Delta t}, y_{t+\Delta t})$ of the oil spill particle at the time $t + \Delta t$ is given by

$$\begin{aligned} x_{t+\Delta t} &= x_t + \frac{\Delta x_p}{\gamma \cos y_t} \\ y_{t+\Delta t} &= y_t + \frac{\Delta y_p}{\gamma}. \end{aligned} \tag{9}$$

The wind field components (i.e., w^u_t and w^v_t) and the current field components (i.e., c^u_t and c^v_t) are crucial factors for maintaining the performance of oil spill drift prediction. The accuracy of the oil spill drift prediction heavily relies on the accuracy of the wind fields and current fields.

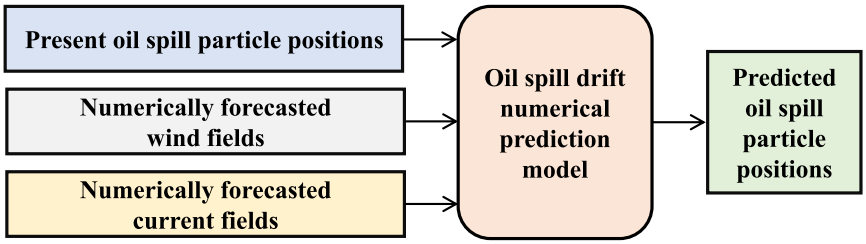

Fig. 4. Basic oil spill drift prediction.

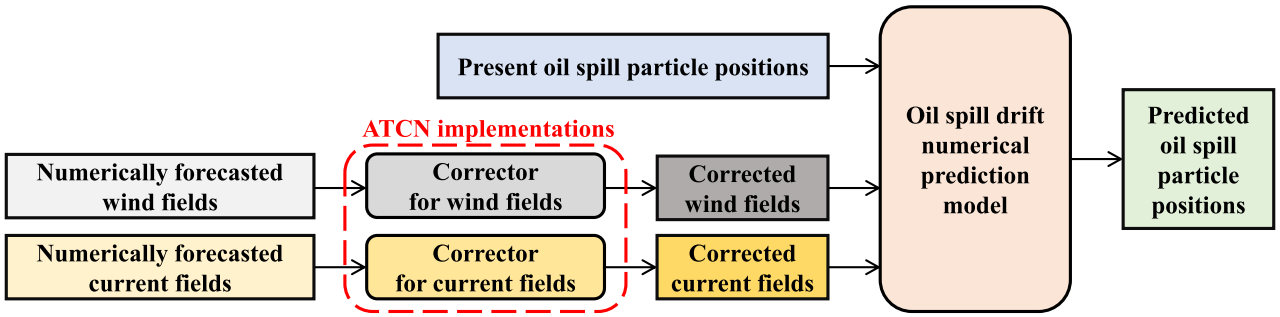

Fig. 5. Sea surface dynamic field correction-based oil spill drift prediction.

Most existing works tend to use numerically forecasted sea surface dynamic fields (i.e., both wind fields and current fields) as inputs of the oil spill drift numerical prediction model. The numerically forecasted sea surface dynamic fields are timely but with limited accuracy. To improve the accuracy of the sea surface dynamic fields while maintaining their timeliness as well, we develop an SDFCP strategy, which is illustrated in Fig. 5.

The SDFCP strategy exploits a well-trained ATCN framework to correct numerically forecasted sea surface dynamic fields into more accurate sea surface dynamic fields (as presented in Section II-E). In practical operations, the ATCNs take a sequence of numerically forecasted sea surface dynamic fields $\{\boldsymbol{F}^f_{t-T_1}, \ldots, \boldsymbol{F}^f_t, \ldots, \boldsymbol{F}^f_{t+T_2}\}$ (wind fields or current fields) as input and output a corrected sea surface dynamic field $\boldsymbol{F}^c_t$ (i.e., a corrected current field or a corrected wind field) at a specific time t. In the novel SDFCP strategy, the corrected current field is used as the current field component c^u_t or c^v_t in (5), and the corrected wind field is used as the wind field component w^u_t or w^v_t in (5). They offer more accurate current field components and wind field components to the oil spill drift numerical prediction model. The predicted oil spill particle positions are obtained according to (5)–(9).

Here, we make two observations. First, the corrected sea surface dynamic fields are more accurate than their corresponding numerically forecasted sea surface dynamic fields, and they are supposed to drive the oil spill drift numerical prediction model to give more accurate oil spill drift prediction results. Second, when the numerically forecasted sea surface dynamic fields are obtained, they are immediately processed by the ATCNs into the corrected sea surface dynamic fields, which enable the timeliness of the oil spill drift prediction. Therefore, the novel SDFCP strategy gives both accurate and timely oil spill drift prediction results.

Our method can be implemented immediately upon observing an oil spill, as the necessary components—the trained corrector and the numerically forecasted sea surface dynamic fields—are both readily available. The corrector is already trained, and the forecasted dynamic fields can be accessed several days in advance.

The overall strategy of enhancing oil spill drift prediction by correcting numerically forecasted sea surface dynamic fields with ATCNs is applicable globally. However, sea surface dynamics can vary significantly between open seas and coastal areas. Therefore, it is essential to train and implement the ATCNs specifically for the region where the strategy will be applied.

IV. Datasets for Symphony and Sanchi Oil Spill Accidents

In this section, we present a dataset of sea surface dynamic fields and a dataset of oil spills, both of which are for Symphony and Sanchi oil spill accidents. The datasets along with the code for implementing the proposed method are released at https://github.com/jiaqilin114/UPC_OilSpill_Track.

A. Dataset: Sea Surface Dynamic Fields

In this section, we present the sea surface dynamic field dataset, including numerically forecasted wind fields, reanalysis wind fields, numerically forecasted current fields, and analysis current fields.

As presented in Table II, the numerically forecasted wind fields are sourced from the NCEP-GFS archive, and the reanalysis wind fields are sourced from the ECMWF-ERA5

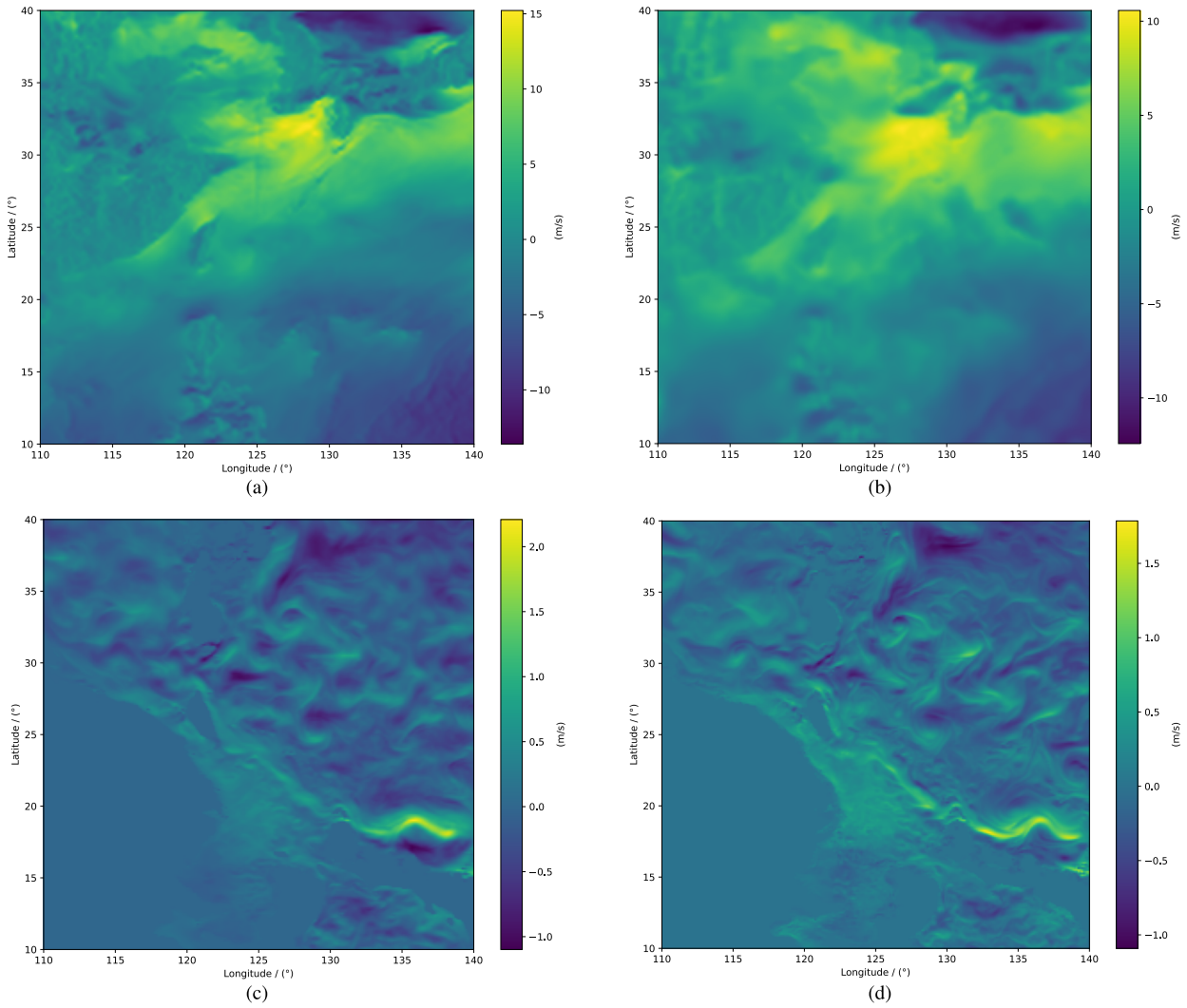

Fig. 6. Sea surface dynamic fields in the u-direction on May 1, 2021 at 00:00 UTC. (a) Numerically forecasted wind field. (b) Reanalysis wind field. (c) Numerically forecasted current field. (d) Analysis current field.

TABLE II
SEA SURFACE DYNAMIC FIELD DATA

Data type	Data source	Spatial resolution	Temporal resolution
Numerically forecasted wind fields	NCEP	0.125° × 0.125°	6 hours
Reanalysis wind fields	ECMWF	0.125° × 0.125°	6 hours
Numerically forecasted current fields	HYCOM	0.125° × 0.125°	6 hours
Analysis current fields	CMEMS	0.125° × 0.125°	6 hours

archive. The numerically forecasted current fields are sourced from the HYCOM-GLBy0.08 archive, and the analysis current fields are sourced from the CMEMS-GOPAF archive. The data region covers the area (40°N, 110°E) to (10°N, 140°E). It covers both from the Symphony and Sanchi oil spill accidents. As presented in Table II, the spatial resolution is set to 0.125° × 0.125° through sampling, and the temporal resolution is set to 6 h. Each dynamic field (i.e., numerically forecasted dynamic field or reanalysis dynamic field) with a size of 241 × 241 × 2 has two components (i.e., u and v). The dynamic fields are described separately as follows.

1) The numerically forecasted wind fields are provided for two periods: January 1–December 31, 2021, and January 1–December 31, 2018. Each period includes 1460 wind fields.
2) The reanalysis wind fields are provided for two periods: January 1–December 31, 2021, and January 1–December 31, 2018. Each period includes 1460 wind fields.

TABLE III
REMOTE SENSING DATA FOR THE SYMPHONY OIL SPILL ACCIDENT

Capture date	File name	Satellite
2021-05-01	S1A_IW_GRDH_1SDV_20210501T095610_20210501T095635_037693_047292_191D	Sentinel-1
2021-05-02	GF1_WFV4_E122.0_N35.0_20210502_L1A0005626723	GF-1
2021-05-05	GF1_WFV1_E121.3_N36.3_20210505_L1A0005631787	GF-1
2021-05-07	S1B_IW_GRDH_1SDV_20210507T095540_20210507T095605_026797_03337C_693E	Sentinel-1

TABLE IV
REMOTE SENSING DATA FOR THE SANCHI OIL SPILL ACCIDENT

Capture date	File name	Satellite
2018-01-18	S2A_MSIL1C_20180118T022021_N0206_R003_T51RYM_20180118T073758	Sentinel-2
2018-01-20	GF1_WFV4_E125.4_N28.4_20180120_L1A0002945335	GF-1

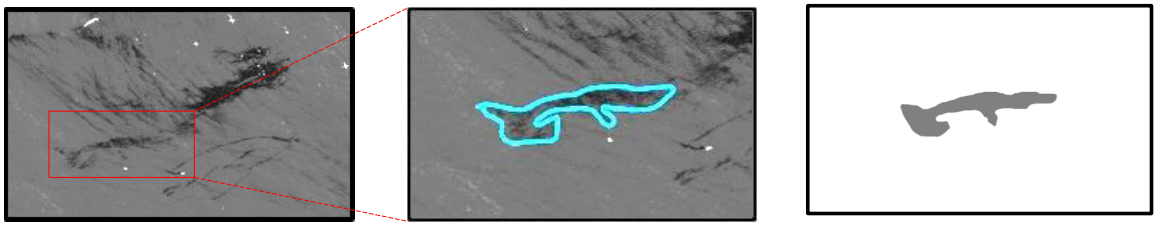

Fig. 7. Symphony oil spill remote sensing data captured by the Sentinel-1 satellite on May 1, 2021 at 09:56 UTC: image, patch, and oil spill position.

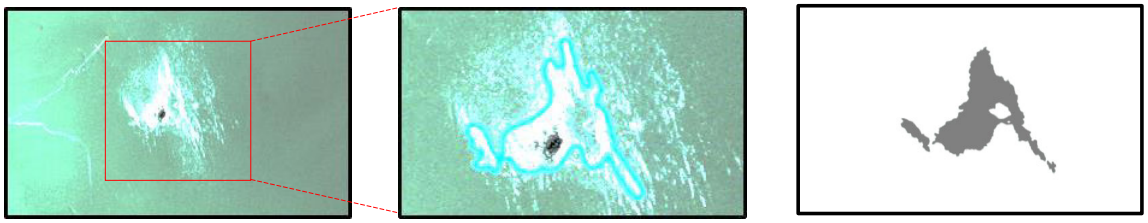

Fig. 8. Symphony oil spill remote sensing data captured by the GF-1 satellite on May 2, 2021 at 10:55 UTC: image, patch, and oil spill position.

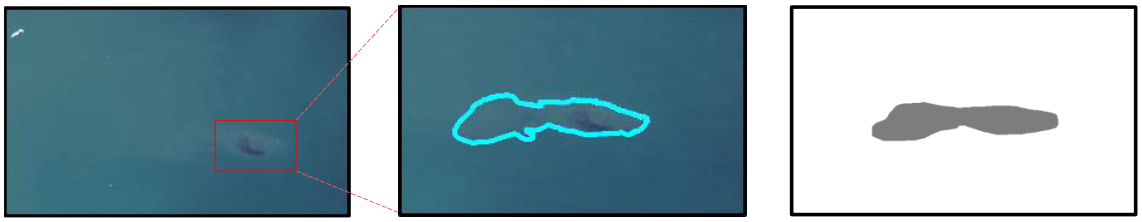

Fig. 9. Symphony oil spill remote sensing data captured by the GF-1 satellite on May 5, 2021, at 10:28 UTC: image, patch, and oil spill position.

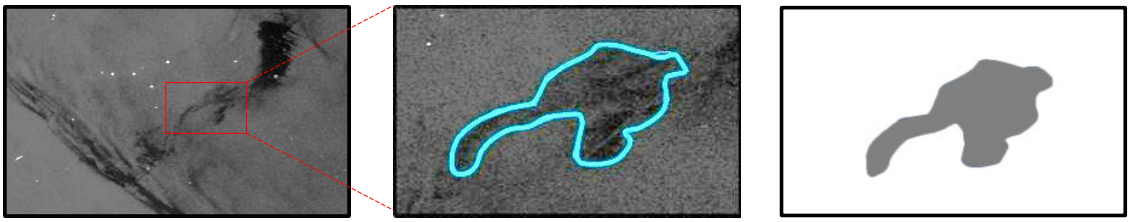

Fig. 10. Symphony oil spill remote sensing data captured by the Sentinel-1 satellite on May 7, 2021, at 09:55 UTC: image, patch, and oil spill position.

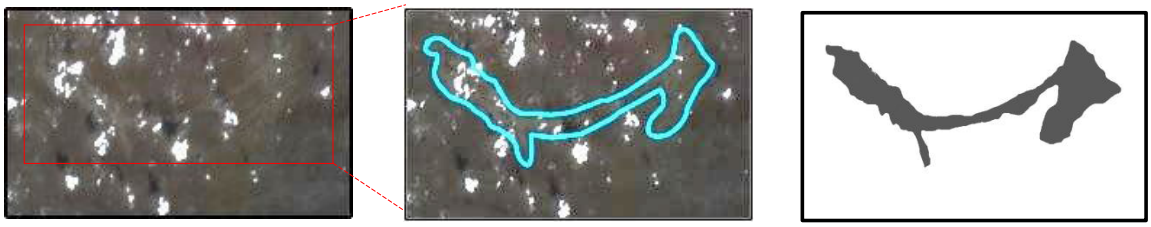

Fig. 11. Sanchi oil spill remote sensing data captured by the Sentinel-2 satellite on January 18, 2018, at 02:20 UTC: image, patch, and oil spill position.

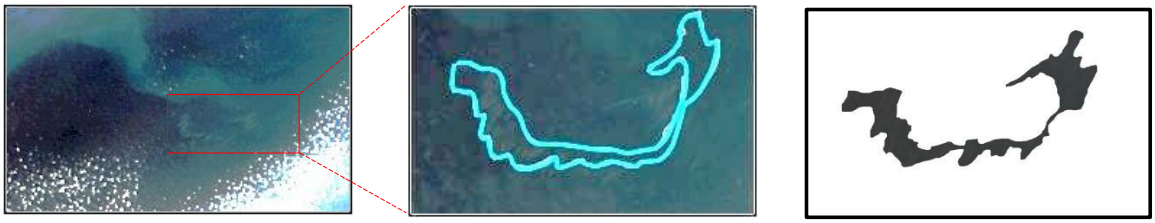

Fig. 12. Sanchi oil spill remote sensing data captured by the GF-1 satellite on January 20, 2018, at 11:17 UTC: image, patch, and oil spill position.

TABLE V
PARAMETER CONFIGURATION FOR THE ATCN FRAMEWORK

	Layer	Filter	Kernel	Padding
C	3DCNN + LReLU	256	3×3	causal
	3DCNN + LReLU	128	3×3	causal
	3DCNN + LReLU	64	3×3	causal
	3DCNN + LReLU	32	3×3	causal
	2DCNN + LReLU	1	1×1	same
D	Conv + LReLU	64	5×5	same
	Conv + LReLU	128	3×3	same
	Conv + LReLU	64	3×3	same
	Conv	1	3×3	same

C refers to the Corrector, D refers to the Discriminator.

3) The numerically forecasted current fields are provided for the period from January 1 to December 31, 2021, comprising a total of 1460 current fields.
4) The analysis current fields are provided for the period from January 1 to December 31, 2021, comprising a total of 1460 current fields.

We present visual examples of the sea surface dynamic fields in the u-direction on May 1, 2021 at 00:00 UTC in Fig. 6. Fig. 6(a) and (b) illustrates the numerically forecasted wind field and the reanalysis wind field, respectively. Fig. 6(c) and (d) illustrates the numerically forecasted current field and the analysis current field, respectively.

In our study, the corrected sea surface dynamic fields have temporal and spatial resolutions of 0.125° and 6 h, respectively, which match the resolutions of the numerically forecasted sea surface dynamic fields. However, our method is equally applicable if numerically forecasted sea surface dynamic fields with higher temporal and spatial resolutions are used, yielding the same solution.

B. Dataset: Oil Spills

In this section, we present the remote sensing dataset for both the Symphony and Sanchi oil spill accidents. Automatic oil spill detection is a crucial but challenging task, especially when oil spill features are unclear. On the other hand, our work focuses on oil spill drift prediction. For this purpose, oil spills are manually detected by experts to provide reliable evidence for validating our oil spill drift prediction strategy.

The dataset includes remote sensing data during the processes of both the Symphony and Sanchi oil spill accidents.

1) *Symphony Oil Spill Accident:* The time range of the remote sensing data is between May 1, 2021 and May 7, 2021. The data were captured at four times. Details of the remote sensing data about the Symphony oil spill accident are presented in Table III.
2) *Sanchi Oil Spill Accident:* The time range of the remote sensing data is between January 18, 2018 and January 20, 2018. The data were captured at two times. Details of the remote sensing data about the Sanchi oil spill accident are presented in Table IV.

Fig. 7 illustrates the remote sensing data captured by the Sentinel-1 satellite on May 1, 2021, at 09:56 UTC, for the Symphony accident. Fig. 8 illustrates the remote sensing data captured by the GF-1 satellite on May 2, 2021, at 10:55 UTC, for the Symphony accident. Fig. 9 illustrates the remote sensing data captured by the GF-1 satellite on May 5, 2021, at 10:28 UTC, for the Symphony accident. Fig. 10 illustrates the remote sensing data captured by the Sentinel-1 satellite on May 7, 2021, at 09:55 UTC, for the Symphony accident. Fig. 11 illustrates the remote sensing data captured by the Sentinel-2 satellite on January 18, 2018, at 02:20 UTC, for the Sanchi accident. Fig. 12 illustrates the remote sensing data captured by the GF-1 satellite on January 20, 2018, at 11:17 UTC, for the Sanchi accident.

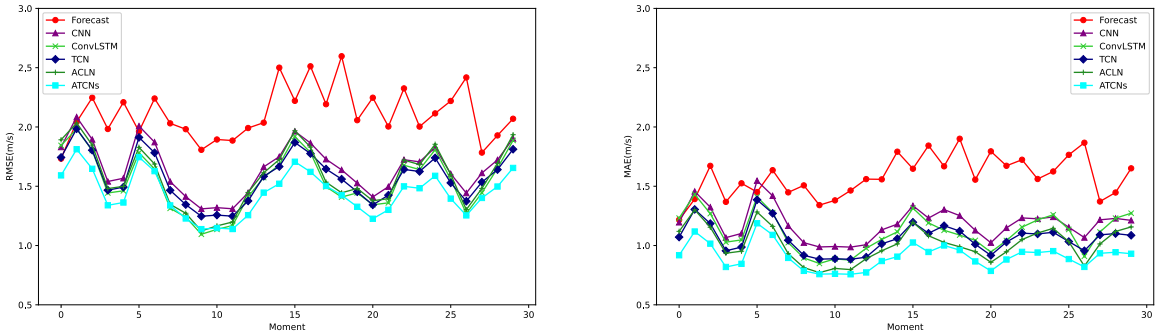

Fig. 13. Wind field correction performances in the u-direction between May 1, 2021 at 00:00 UTC and May 8, 2021 at 06:00 UTC. (a) RMSE at 30 moments with 6-h intervals. (b) MAE at 30 moments with 6-h intervals.

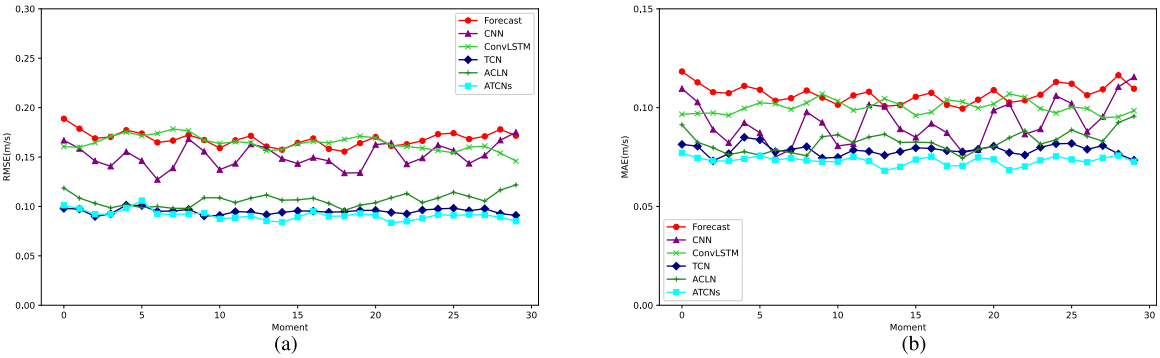

Fig. 14. Current field correction performances in the u-direction between May 1, 2021 at 00:00 UTC and May 8, 2021 at 06:00 UTC. (a) RMSE at 30 moments with 6-h intervals. (b) MAE at 30 moments with 6-h intervals.

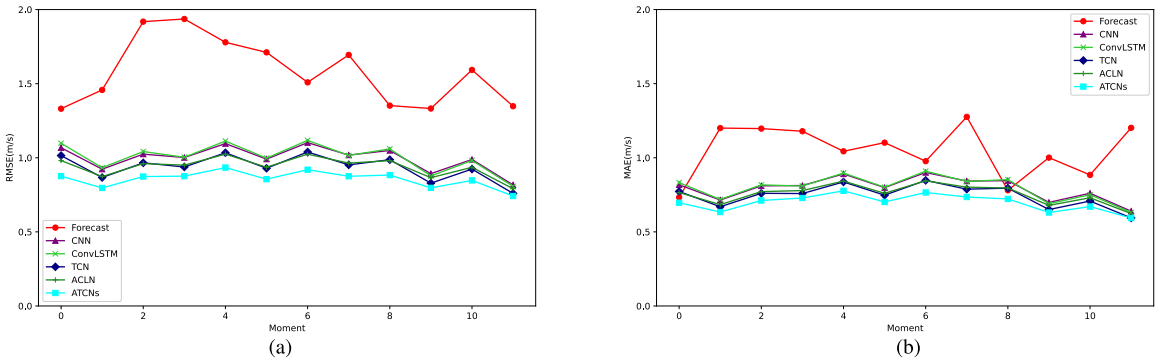

Fig. 15. Wind field correction performances in the u-direction between January 18, 2018 at 00:00 UTC and January 20, 2018 18:00 UTC. (a) RMSE at 12 moments with 6-h intervals. (b) MAE at 12 moments with 6-h intervals.

V. Experimental Evaluations

This section comprehensively evaluates our novel oil spill drift prediction strategy through extensive experiments on the Symphony and Sanchi oil spill accidents, specifically focusing on the efficacy of our strategy that incorporates corrections to wind and current fields via the ATCN framework. Synthetic aperture radar (SAR) remote sensing data and optical remote sensing data from Sentinel-1, Sentinel-2, and GF1 presented in Section IV-B are used for validating the oil spill drift prediction results.

A. Experimental Settings

We describe the settings and metrics used in our experiments. Our method is implemented in Python3 on two Intel Xeon Gold 5218R CPUs and NVIDIA Geforce V100 GPUs, using TensorFlow 1.15.0.

1) Sea Surface Dynamic Field Correction: For evaluating the performance of the ATCN framework for sea surface dynamic field correction, we set the parameters for training the ATCNs in the experiments as follows. The number of 3DCNN modules is $L = 4$. The input sequence length ($T_1 + T_2 + 1$) is set to 4, where $T_1 = 2$ and $T_2 = 1$. The learning rate is 0.0005. Both the corrector and the discriminator in the ATCNs are trained using the Adam optimizer. Both the balance parameters λ_1 and λ_2 are set to 10. The parameter configuration of the ATCN framework is presented in Table V.

We use the data presented in Section IV-A for experiments. The 1430 wind fields from January 1 to May 1, 2021, and from May 8 to December 31, 2021, are used for training. The

30 wind fields from May 1 to May 8 are used to test the correction performance. The 1430 current fields from January 1 to May 1, 2021, and from May 8 to December 31, 2021, are used for training. The 30 current fields from May 1 to May 8 are used to test the correction performance. The 1448 wind fields from January 1 to January 18, 2018, and from January 20 to December 31, 2018, are used for training. The 12 wind fields from January 18 to January 20 are used to test the correction performance.

We use the following quantitative evaluation metrics, to evaluate the sea surface dynamic field correction performance.

Root-mean-squared error (RMSE) is commonly used as an evaluation metric for errors, and it is calculated as follows:

$$\mathrm{RMSE} = \sqrt{\frac{1}{MN}\sum_{m=1}^{M}\sum_{n=1}^{N}\left[\boldsymbol{F}_t^c(m,n) - \boldsymbol{F}_t^r(m,n)\right]^2}. \quad (10)$$

Mean absolute error (MAE) is also commonly used as an evaluation metric for errors, and it is calculated as follows:

$$\mathrm{MAE} = \frac{1}{MN}\sum_{m=1}^{M}\sum_{n=1}^{N}\left|\boldsymbol{F}_t^c(m,n) - \boldsymbol{F}_t^r(m,n)\right|. \quad (11)$$

2) Oil Spill Drift Prediction: The experimental parameters are determined through rigorous empirical tests and set in terms of $\alpha_w = 0.03$, $\alpha_c = 1$, $E_r = 0.005$, $\mu = 12$, and $\gamma = 111$ km.

We use the remote sensing dataset presented in Section IV-B for experiments. We use remote sensing data to capture the initial and final positions of an oil spill drift trajectory segment. For the Symphony oil spill accident, we use two oil spill drift trajectory segments to evaluate the predictions. Figs. 7 and 8 gives the initial and final situations of the first drift trajectory segment depicted by the remote sensing data, respectively. Figs. 9 and 10 gives the initial and final situations of the second oil spill drift trajectory segment depicted by the remote sensing data, respectively. For the Sanchi oil spill accident, we use one segment of the oil spill drift trajectory to evaluate the prediction. Figs. 11 and 12 gives the initial and final situations of the drift trajectory segment depicted by the remote sensing data, respectively.

To assess prediction accuracy, we compare the predicted oil spill region with the oil spill region captured by the remote sensing data at the end of the trajectory segment. We evaluate the oil spill drift prediction performance by measuring the distance between the center point of the predicted oil spill region and that of the ground-truth region. This distance serves as the error metric for our assessment.

B. Sea Surface Dynamic Field Correction

In this section, we evaluate the performance of the ATCN framework by comparing its correction results with four different deep learning networks: CNN, ConvLSTM [60], temporal convolutional network [61], and adversarial ConvLSTM network [56]. These four different deep learning networks are separately trained and tested with the same dataset, learning rate, and optimizer as the ATCNs. We use the values of RMSE and MAE in the u-direction of the sea surface dynamic fields for evaluation.

TABLE VI
WIND FIELD CORRECTION PERFORMANCES IN u-DIRECTION BETWEEN MAY 1, 2021 AT 00:00 UTC AND MAY 8, 2021 AT 06:00 UTC

Type	Network	RMSE	MAE
Wind	Forecasted	2.1077	1.5801
	CNN	1.6569	1.1862
	ConvLSTM	1.5424	1.1139
	TCN	1.5780	1.0626
	ACLN	1.5820	1.0127
	ATCNs	**1.4407**	**0.9108**

TABLE VII
CURRENT FIELD CORRECTION PERFORMANCES IN u-DIRECTION BETWEEN MAY 1, 2021 AT 00:00 UTC AND MAY 8, 2021 AT 06:00 UTC

Type	Network	RMSE	MAE
Current	Forecasted	0.1684	0.1070
	CNN	0.1512	0.0924
	ConvLSTM	0.1640	0.1002
	TCN	0.0950	0.0785
	ACLN	0.1064	0.0828
	ATCNs	**0.0912**	**0.0760**

TABLE VIII
WIND FIELD CORRECTION PERFORMANCES IN u-DIRECTION BETWEEN MAY 18, 2018 AT 00:00 UTC AND MAY 20, 2018 AT 18:00 UTC

Type	Network	RMSE	MAE
Wind	Forecasted	1.4298	1.0479
	CNN	0.9975	0.7944
	ConvLSTM	1.0037	0.7958
	TCN	0.9364	0.7440
	ACLN	0.9405	0.7563
	ATCNs	**0.8562**	**0.6972**

Fig. 13 gives the numerically forecasted wind correction performances of five deep learning networks. The low curve indicates good correction performance. Fig. 13(a) and (b) shows that the five networks achieve different levels of wind field correction, and the correction performance of the ATCNs is better than the other four networks. Table VI presents

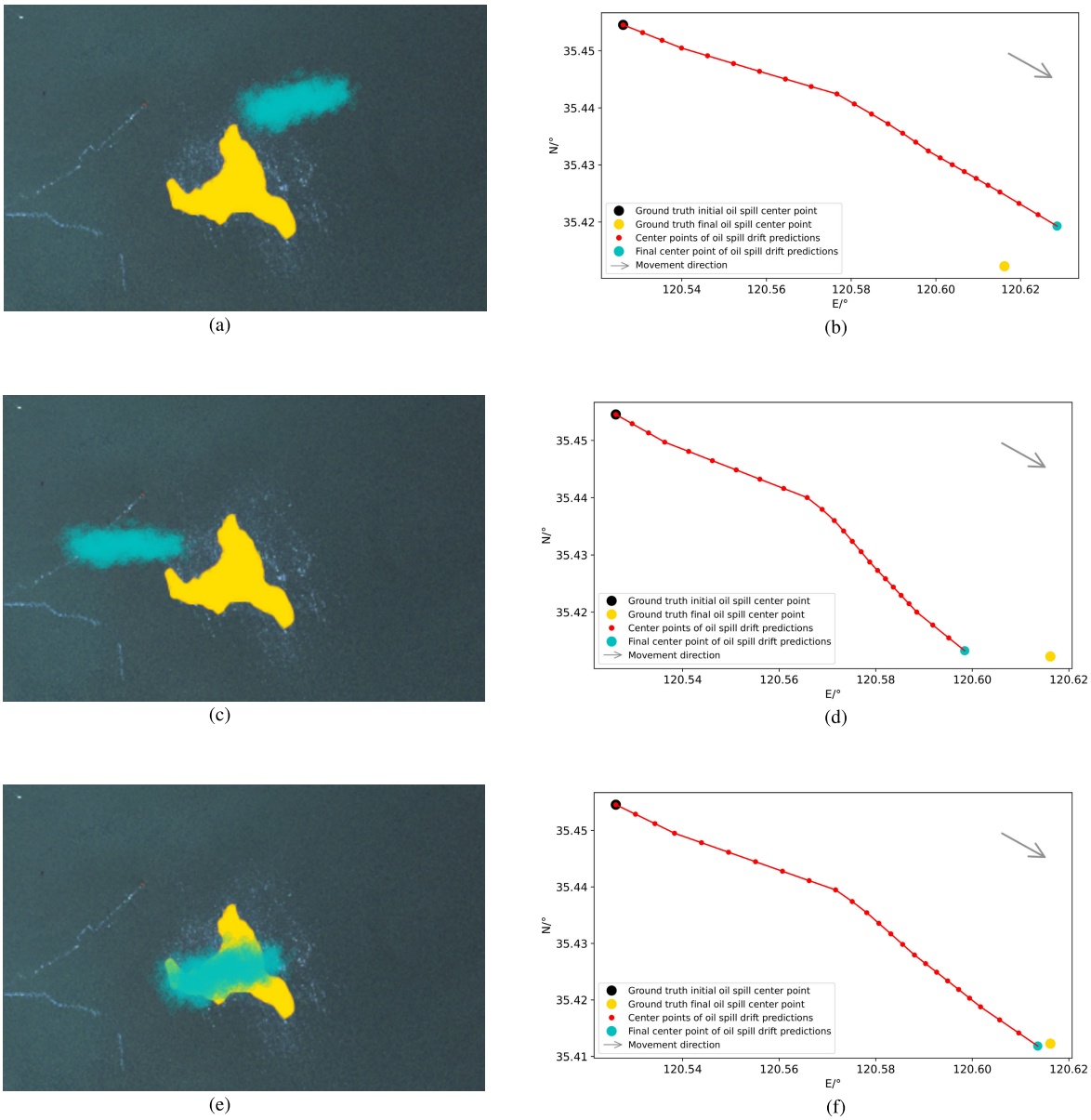

Fig. 16. Prediction results for the Symphony oil spill drift first trajectory segment, driven by different dynamic fields. In each of (a), (c), and (e), golden region indicates the ground-truth final oil spill region of the drift, and the cyan region indicates the predicted final oil spill region of the drift. In each of (b), (d), and (f), black point indicates the center point of the ground-truth initial oil spill region of the drift, the golden point indicates the center point the ground-truth finial oil spill region of the drift, the cyan point indicates the center point of the predicted finial oil spill region of the drift, the red points dynamically show the predicted drift trajectory, and the gray arrow indicates the direction of the oil spill drift.

the wind field correction performances. It confirms that the correction performances of the ATCNs are better than those of the other four methods.

Fig. 14 gives the numerically forecasted current correction performances of five deep learning networks. Fig. 14(a) and (b) shows that the five networks achieve different levels of current field correction, and the correction performance of the ATCNs is better than the other four networks. Table VII presents the current field correction performances. It confirms that the correction performances of the ATCNs are better than those of the other four methods.

Fig. 15 gives the numerically forecasted wind correction performances of five deep learning networks. Fig. 15(a) and (b) shows that the five networks achieve different levels of wind field correction, and the correction performance of the ATCNs is better than the other four networks. Table VIII presents the wind field correction performances. It confirms that the correction performances of the ATCNs are better than those of the other four methods.

Although our method achieves state-of-the-art performance in the experimental comparisons, it faces challenges in experimental configurations. First, the time intervals of the sea surface dynamic fields for training and testing the ATCNs are continuous, with no time gaps. A key challenge for future experiments is how to train the ATCNs using historical data and then implement them with present data which may have

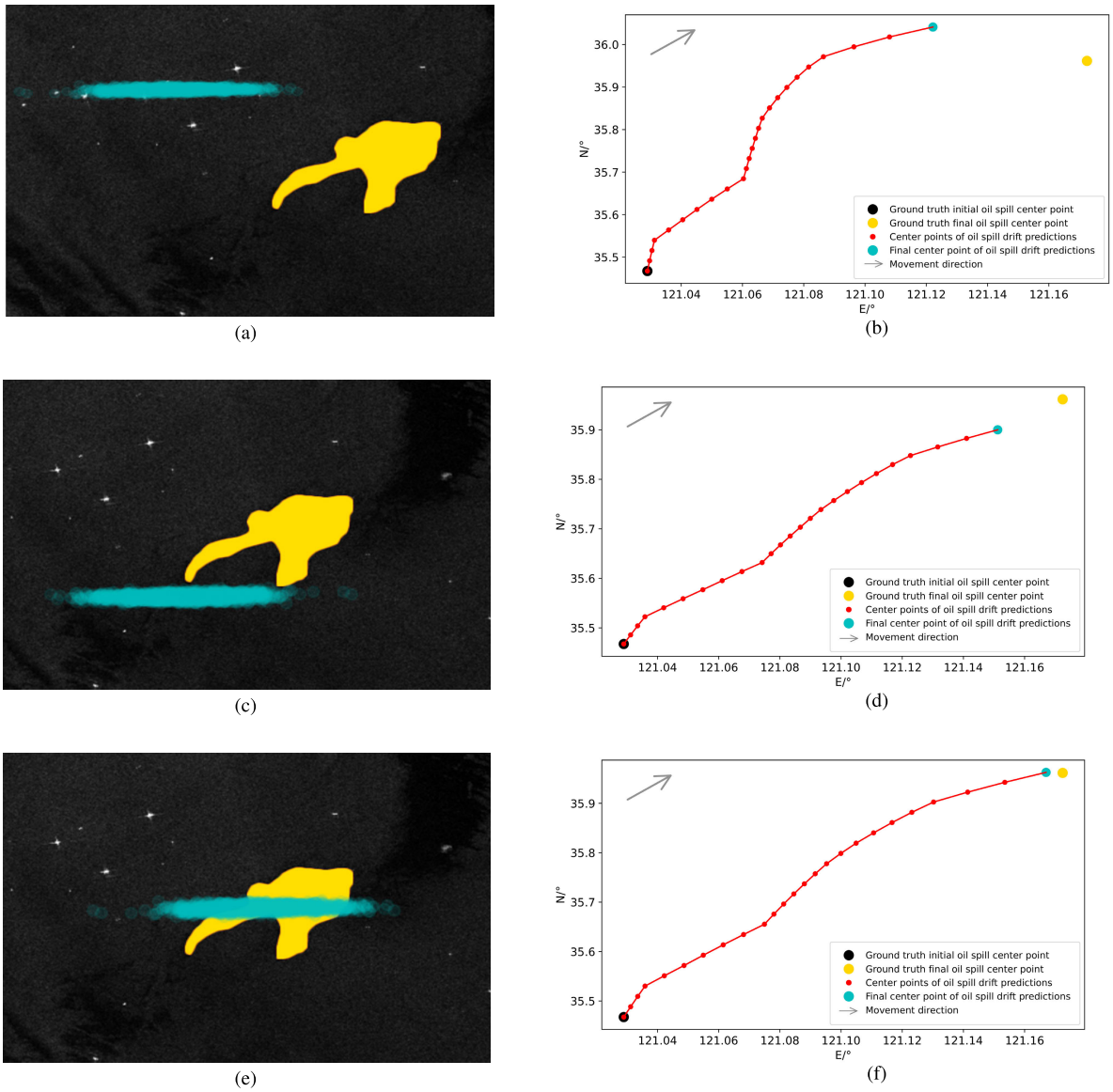

Fig. 17. Symphony oil spill drift second trajectory segment prediction results driven by different dynamic fields. The colors and symbols have the same meanings as those in Fig. 16. (a) Numerically forecasted wind and current fields. (b) Numerically forecasted wind and current fields. (c) Corrected wind fields and numerically forecasted current fields. (d) Corrected wind fields and numerically forecasted current fields. (e) Corrected wind and current fields. (f) Corrected wind and current fields.

time gaps from the historical data. Second, there are several hyperparameters involved in training the ATCNs, and determining how to tune them with minimal intervention remains another challenge.

C. Oil Spill Drift Prediction

We commence by evaluating the effectiveness of the SDFCP strategy for the Symphony oil spill accident. We assume that the two oil spill drift trajectory segments started at the moments when the remote sensing images shown in Figs. 7 and 9 were acquired, separately. Section V-B has already demonstrated the efficacy of the ATCN framework, which shows superior performance in correcting sea surface dynamic fields from May 1, 2021 at 00:00 UTC to May 8, 2021 at 06:00 UTC. We conduct the experiments using the numerically forecasted sea surface dynamic fields and the corrected sea surface dynamic fields separately as the inputs of the oil spill drift numerical prediction model presented in Section III and obtain the following results.

Fig. 16 presents the drift prediction results for the first trajectory segment of the Symphony oil spill. Fig. 16(a) and (b) displays the prediction results based on numerically forecasted wind and current fields. Fig. 16(c) and (d) shows the prediction results based on corrected wind fields and numerically forecasted current fields. Fig. 16(e) and (f) shows the prediction results using the corrected wind and current fields. For the first trajectory segment of the Symphony oil spill drift, based on remote sensing data, the circumscribed circle diameter of the initial oil spill region is approximately 2270 m (estimated based on remote sensing data in Fig. 7), while the final oil spill region measures around 2525 m (estimated based on remote sensing data in Fig. 8). The drift observed in our

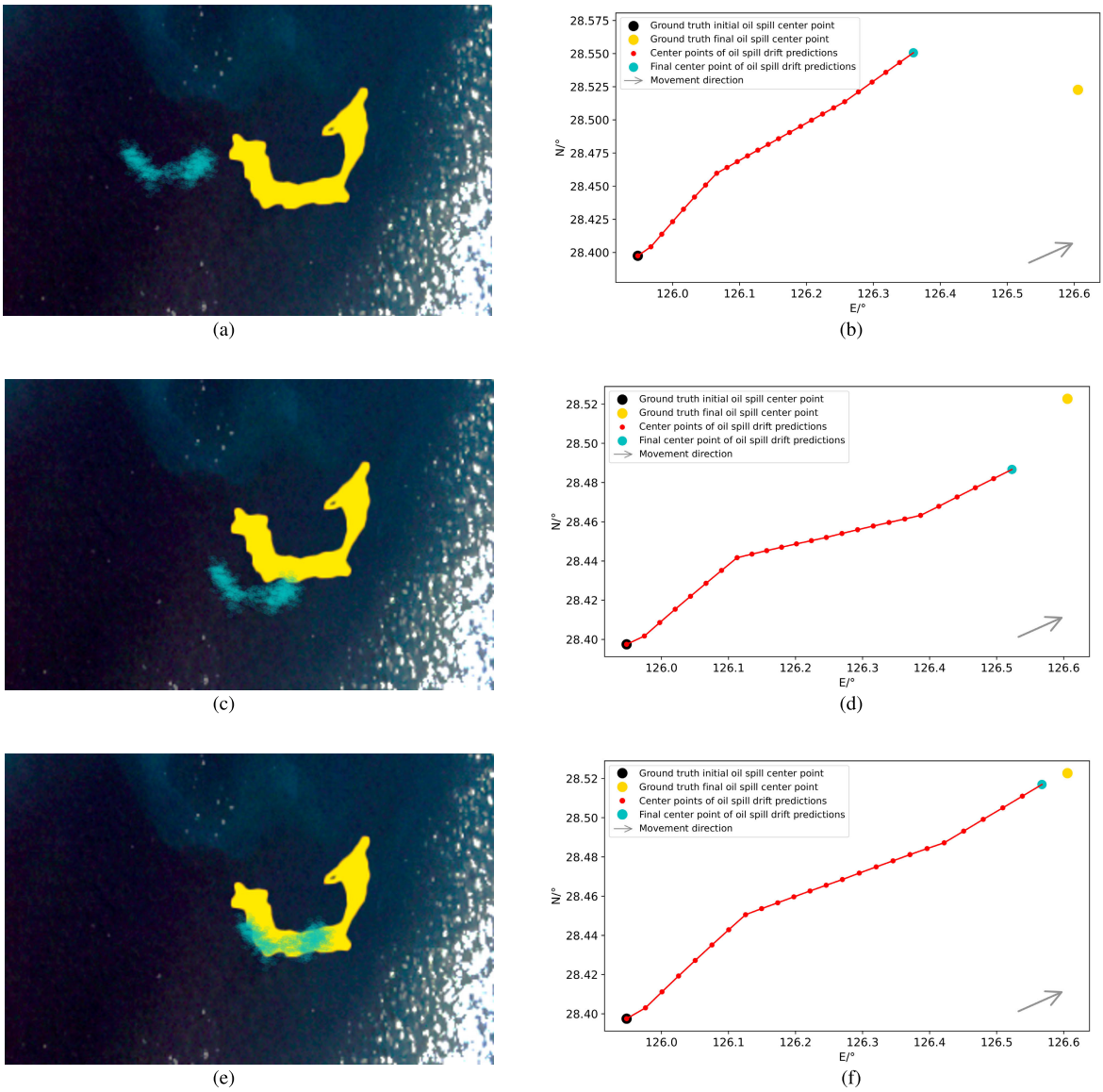

Fig. 18. Sanchi oil spill drift prediction results driven by different dynamic fields. The colors and symbols have the same meanings as those in Fig. 16. (a) Numerically forecasted wind and current fields. (b) Numerically forecasted wind and current fields. (c) Corrected wind fields and numerically forecasted current fields. (d) Corrected wind fields and numerically forecasted current fields. (e) Corrected wind and current fields. (f) Corrected wind and current fields.

experiments lasted for about 25 h. The error in the center point of the predicted final oil spill region has been reduced from 1371 m, based on numerically forecasted sea surface dynamic fields, to 242 m when using corrected sea surface dynamic fields.

Fig. 17 presents the drift prediction results for the second trajectory segment of the Symphony oil spill. Fig. 17(a) and (b) displays the prediction results based on numerically forecasted wind and current fields. Fig. 17(c) and (d) shows the prediction results based on corrected wind fields and numerically forecasted current fields. Fig. 17(e) and (f) shows the prediction results using the corrected wind and current fields. For the second trajectory segment of the Symphony oil spill drift, the circumscribed circle diameter of the initial oil spill region is approximately 1360 m (estimated based on remote sensing data in Fig. 9), while the final oil spill region measures around 1800 m (estimated based on remote sensing data in Fig. 10). The drift observed in our experiments lasted for about 46 h. The error in the center point of the predicted final oil spill region has been reduced from 9924 m, based on numerically forecasted sea surface dynamic fields, to 521 m when using corrected sea surface dynamic fields.

We observe in Figs. 16 and 17 that the prediction results using the ATCNs-corrected wind and current fields more closely match the ground-truth oil spill drifts than those based on the numerically forecasted wind fields and current fields. This highlights the effectiveness of the dynamic field corrections by the ATCNs in enhancing prediction accuracy. Although the prediction results in Figs. 16(f) and 17(f) are better than those in Figs. 16(b) and 17(b), they still exhibit some differences from the ground-truth drift results. One possible reason is the minimum temporal resolution of the wind and

TABLE IX
ABLATION ANALYSIS FOR SEA SURFACE DYNAMIC FIELD CORRECTION PERFORMANCES IN u-DIRECTION BETWEEN MAY 1, 2021 AT 00:00 UTC AND MAY 8, 2021 AT 06:00 UTC

Network	Adversarial mechanism	Wind field correction (MAE)	Current field correction (MAE)
TCN	×	1.0626	0.0785
ATCNs	✓	0.9108	0.0760

TABLE X
ABLATION ANALYSIS FOR OIL SPILL DRIFT PREDICTION

Numerically forecasted dynamic fields		Corrector		Prediction results
Wind fields	Current fields	For wind fields	For current fields	
✓	✓	×	×	Figs. 16(a), 16(b), 17(a), 17(b), 18(a), and 18(b)
✓	✓	✓	×	Figs. 16(c), 16(d), 17(c), 17(d), 18(c), and 18(d)
✓	✓	✓	✓	Figs. 16(e), 16(f), 17(e), 17(f), 18(e), and 18(f)

current fields being 6 h that hinders more refined results. This suggests that improving the temporal resolution of numerically forecasted sea surface dynamic fields can reasonably enhance the accuracy of oil spill drift prediction.

We then evaluate the effectiveness of the SDFCP strategy for the Sanchi oil spill accident. We assume that the oil spill drift trajectory started at the moment when the remote sensing image shown in Fig. 11 was acquired. Section V-B has already demonstrated the efficacy of the ATCN framework, which shows superior performance in correcting sea surface dynamic fields from January 18, 2018, at 00:00 UTC to January 21, 2018, at 18:00 UTC. We conduct the experiments using the numerically forecasted dynamic fields and the corrected dynamic fields separately as the inputs of the oil spill drift numerical prediction model and obtain the following results.

Fig. 18 presents the drift prediction results for the Sanchi oil spill drift trajectory. Fig. 18(a) and (b) displays the prediction results based on numerically forecasted wind and current fields. Fig. 18(c) and (d) shows the prediction results based on the corrected wind fields and numerically forecasted current fields. Fig. 18(e) and (f) shows the prediction results using corrected wind and current fields. For the trajectory segment of the Sanchi oil spill drift, the circumscribed circle diameter of the initial oil spill region is approximately 8 km (estimated based on remote sensing data in Fig. 11), while the final oil spill region measures around 17 km (estimated based on the remote sensing data in Fig. 12). The drift observed in our experiments lasted for about 57 h. The error in the center point of the predicted final oil spill region has been reduced from 24 km, based on numerically forecasted sea surface dynamic fields, to 6 km when using corrected sea surface dynamic fields.

We observe in Fig. 18 that the prediction results using the ATCNs-corrected wind and current fields more closely match the ground-truth oil spill drift than those based on the numerically forecasted wind fields and current fields. This highlights again the effectiveness of the dynamic field corrections by the ATCNs in enhancing prediction accuracy.

D. Ablation Analysis

In this section, we conduct an ablation analysis to assess the performance improvements achieved using the adversarial learning strategy within the corrector, as well as to evaluate the enhancement in oil spill drift prediction provided by the corrector.

Table IX gives the results of using or not using the adversarial learning strategy. TCN represents the model that does not use the adversarial learning strategy, while ATCNs represent the models that apply the adversarial learning strategy to TCN. For TCN, the MAE for wind field correction performances is 1.0626 and the MAE for current field correction performances is 0.0785. For ATCNs, the MAE for wind field correction performances is 0.9108 and the MAE for current field correction performances is 0.0760. It is validated that the adversarial learning strategy has great gain to improve the correction performance of the corrector. The correction performances of the wind fields and current fields in ATCNs are improved by 14.2857% and 3.1847%, compared with TCN, respectively.

Table X gives the prediction results of using or not using the corrector to oil spill prediction. It is observed that not using corrector for wind fields and current fields gives the worst prediction results, as demonstrated in Figs. 16(a) and (b), 17(a) and (b), and 18(a) and (b). When the wind field corrector is used, the prediction results are improved, as demonstrated in Figs. 16(c) and (d), 17(c) and (d), and 18(c) and (d). Using corrector for both wind and current fields leads to the best prediction results, as demonstrated in Figs. 16(e) and (f), 17(e) and (f), and 18(e) and (f). The ablation analysis indicates that applying correctors to numerically forecasted sea surface dynamic fields significantly enhances prediction accuracy. This improvement is particularly notable when two separate correctors are used for the wind and current fields.

In summary, the ablation analysis highlights the importance of both the adversarial learning strategy and the corrector in enhancing oil spill drift prediction performance. The adversarial learning strategy improves the performance of the corrector,

and on this basis improves the performance of oil spill drift prediction.

VI. Concluding Remark

This study has developed an ATCN framework to enhance the accuracy of sea surface dynamic fields, subsequently enhancing the accuracy of oil spill drift prediction. Through rigorous empirical analysis, particularly with the Symphony and Sanchi oil spill accidents, the ATCN framework-based correction approach has demonstrated superior efficacy over numerical forecast, substantially reducing prediction errors. The methodology underscores the potential of integrating advanced deep learning algorithms with environmental modeling to augment the efficacy of emergency response strategies and environmental preservation initiatives.

Although the ATCN framework-based correction approach has innovatively explored deep learning for correcting sea surface dynamic field forecasts toward timely and accurate predicting oil spill drift, it is still in its pioneering stage and has limitations. Currently, it focuses primarily on dynamic field factors. Future research will address this by incorporating additional factors such as oil spill types, temperature, weathering processes, thickness, and concentration, aiming to further enhance the precision of drift predictions.

References

[1] C. Dearden, T. Culmer, and R. Brooke, "Performance measures for validation of oil spill dispersion models based on satellite and coastal data," *IEEE J. Ocean. Eng.*, vol. 47, no. 1, pp. 126–140, Jan. 2022.

[2] Y. Wang et al., "Environmental impact and recovery of the Bohai Sea following the 2011 oil spill," *Environ. Pollut.*, vol. 263, Aug. 2020, Art. no. 114343.

[3] C. Bayındır, J. D. Frost, and C. F. Barnes, "Assessment and enhancement of SAR noncoherent change detection of sea-surface oil spills," *IEEE J. Ocean. Eng.*, vol. 43, no. 1, pp. 211–220, Jan. 2018.

[4] P. Ren, M. Xu, Y. Yu, F. Chen, X. Jiang, and E. Yang, "Energy minimization with one dot fuzzy initialization for marine oil spill segmentation," *IEEE J. Ocean. Eng.*, vol. 44, no. 4, pp. 1102–1115, Oct. 2019.

[5] B. Zhang, X. Li, W. Perrie, and O. Garcia-Pineda, "Compact polarimetric synthetic aperture radar for marine oil platform and slick detection," *IEEE Trans. Geosci. Remote Sens.*, vol. 55, no. 3, pp. 1407–1423, Mar. 2017.

[6] A. Trucco et al., "Compounding approaches for wind prediction from underwater noise by supervised learning," *IEEE J. Ocean. Eng.*, vol. 47, no. 4, pp. 1172–1187, Oct. 2022.

[7] V. Raimondi, L. Palombi, D. Lognoli, A. Masini, and E. Simeone, "Experimental tests and radiometric calculations for the feasibility of fluorescence LiDAR-based discrimination of oil spills from UAV," *Int. J. Appl. Earth Observ. Geoinf.*, vol. 61, pp. 46–54, Sep. 2017.

[8] P. Qi and M. Du, "Multi-factor evaluation indicator method for the risk assessment of atmospheric and oceanic hazard group due to the attack of tropical cyclones," *Int. J. Appl. Earth Observ. Geoinf.*, vol. 68, pp. 1–7, Jun. 2018.

[9] Z. Ma, L. P. Riishøjgaard, M. Masutani, J. S. Woollen, and G. D. Emmitt, "Impact of different satellite wind LiDAR telescope configurations on NCEP GFS forecast skill in observing system simulation experiments," *J. Atmos. Ocean. Technol.*, vol. 32, no. 3, pp. 478–495, Mar. 2015.

[10] W. Zhuo et al., "Crop yield prediction using MODIS LAI, TIGGE weather forecasts and WOFOST model: A case study for winter wheat in Hebei, China during 2009–2013," *Int. J. Appl. Earth Observ. Geoinf.*, vol. 106, Feb. 2022, Art. no. 102668.

[11] R. Kistler et al., "The NCEP–NCAR 50–Year reanalysis: Monthly means CD–ROM and documentation," *Bull. Amer. Meteorolog. Soc.*, vol. 82, no. 2, pp. 247–267, Feb. 2001.

[12] D. A. Mayer, R. H. Weisberg, L. Zheng, and Y. Liu, "Winds on the West Florida Shelf: Regional comparisons between observations and model estimates," *J. Geophys. Res., Oceans*, vol. 122, no. 2, pp. 834–846, Feb. 2017.

[13] M. Kanamitsu et al., "NCEP–DOE AMIP-II reanalysis (R-2)," *Bull. Amer. Meteorolog. Soc.*, vol. 83, no. 11, pp. 1631–1644, Nov. 2002.

[14] S. M. Uppala et al., "The ERA-40 reanalysis," *Quart. J. Roy. Meteorolog. Soc.*, vol. 131, no. 612, pp. 2961–3012, 2005.

[15] D. P. Dee et al., "The ERA-interim reanalysis: Configuration and performance of the data assimilation system," *Quart. J. Roy. Meteorol. Soc.*, vol. 137, no. 656, pp. 553–597, 2011.

[16] M. Nogueira, "Inter-comparison of ERA-5, ERA-interim and GPCP rainfall over the last 40 years: Process-based analysis of systematic and random differences," *J. Hydrol.*, vol. 583, Apr. 2020, Art. no. 124632.

[17] I. Staffell and S. Pfenninger, "Using bias-corrected reanalysis to simulate current and future wind power output," *Energy*, vol. 114, pp. 1224–1239, Nov. 2016.

[18] G. Zodiatis et al., "Oil spill forecasting (prediction)," *J. Mar. Res.*, vol. 75, no. 6, pp. 923–953, Nov. 2017.

[19] A. J. Abascal, S. Castanedo, R. Mínguez, R. Medina, Y. Liu, and R. H. Weisberg, "Stochastic Lagrangian trajectory modeling of surface drifters deployed during the Deepwater Horizon oil spill," in *Proc. 38th Arctic Mar. Oilspill Program (AMOP) Tech. Seminar.* Ottawa, ON, Canada: Environment Canada, Jan. 2015, pp. 77–91.

[20] Y. Liu, A. MacFadyen, Z.-G. Ji, and R. H. Weisberg, "Monitoring and modeling the Deepwater Horizon oil spill: A record-breaking enterprise," *Geophys. Monograph Ser.*, vol. 195, p. 271, Jan. 2011.

[21] Y. Liu, R. H. Weisberg, C. Hu, and L. Zheng, "Tracking the Deepwater Horizon oil spill: A modeling perspective," *EOS, Trans. Amer. Geophys. Union*, vol. 92, no. 6, pp. 45–46, Feb. 2011.

[22] Y. Y. Liu, R. H. R. H. Weisberg, C. C. Hu, and L. L. Zheng, "Trajectory forecast as a rapid response to the Deepwater Horizon oil spill," in *Monitoring and Modeling the Deepwater Horizon Oil Spill: A Record-Breaking Enterprise*. Washington, DC, USA: American Geophysical Union, 2011, pp. 153–165.

[23] A. Berry, T. Dabrowski, and K. Lyons, "The oil spill model OILTRANS and its application to the Celtic Sea," *Mar. Pollut. Bull.*, vol. 64, no. 11, pp. 2489–2501, Nov. 2012.

[24] Y. Cheng et al., "Monitoring of oil spill trajectories with COSMO-SkyMed X-band SAR images and model simulation," *IEEE J. Sel. Topics Appl. Earth Observ. Remote Sens.*, vol. 7, no. 7, pp. 2895–2901, Jul. 2014.

[25] C. E. Jones et al., "Measurement and modeling of oil slick transport," *J. Geophys. Res., Oceans*, vol. 121, no. 10, pp. 7759–7775, Oct. 2016.

[26] J. Röhrs et al., "The effect of vertical mixing on the horizontal drift of oil spills," *Ocean Sci.*, vol. 14, no. 6, pp. 1581–1601, Dec. 2018.

[27] C. Brekke, M. M. Espeseth, K. Dagestad, J. Röhrs, L. R. Hole, and A. Reigber, "Integrated analysis of multisensor datasets and oil drift simulations—A free-floating oil experiment in the open ocean," *J. Geophys. Res., Oceans*, vol. 126, no. 1, Jan. 2021, Art. no. e2020JC016499.

[28] F. Cassola and M. Burlando, "Wind speed and wind energy forecast through Kalman filtering of numerical weather prediction model output," *Appl. Energy*, vol. 99, pp. 154–166, Nov. 2012.

[29] C. P. Sweeney, P. Lynch, and P. Nolan, "Reducing errors of wind speed forecasts by an optimal combination of post-processing methods," *Meteorolog. Appl.*, vol. 20, no. 1, pp. 32–40, Mar. 2013.

[30] A. M. Ishak, R. Remesan, P. K. Srivastava, T. Islam, and D. Han, "Error correction modelling of wind speed through hydro-meteorological parameters and mesoscale model: A hybrid approach," *Water Resour. Manage.*, vol. 27, no. 1, pp. 1–23, Jan. 2013.

[31] P. Lauret, M. Diagne, and M. David, "A neural network post-processing approach to improving NWP solar radiation forecasts," *Energy Proc.*, vol. 57, pp. 1044–1052, May 2014.

[32] L. Zjavka, "Wind speed forecast correction models using polynomial neural networks," *Renew. Energy*, vol. 83, pp. 998–1006, Nov. 2015.

[33] Y. Liu, Y. Wang, L. Li, S. Han, and D. Infield, "Numerical weather prediction wind correction methods and its impact on computational fluid dynamics based wind power forecasting," *J. Renew. Sustain. Energy*, vol. 8, no. 3, May 2016, Art. no. 033302.

[34] S. Buhan, Y. Özkazanç, and I. Çadirci, "Wind pattern recognition and reference wind mast data correlations with NWP for improved wind-electric power forecasts," *IEEE Trans. Ind. Informat.*, vol. 12, no. 3, pp. 991–1004, Jun. 2016.

[35] X. Chen, W. Huang, and M. C. Haller, "A novel scheme for extracting sea surface wind information from rain-contaminated X-band marine radar images," *IEEE J. Sel. Topics Appl. Earth Observ. Remote Sens.*, vol. 14, pp. 5220–5234, 2021.
[36] R. Tang, Y. Ning, C. Li, W. Feng, Y. Chen, and X. Xie, "Numerical forecast correction of temperature and wind using a single-station single-time spatial LightGBM method," *Sensors*, vol. 22, no. 1, p. 193, Dec. 2021.
[37] L. Han et al., "A deep learning method for bias correction of ECMWF 24–240 h forecasts," *Adv. Atmos. Sci.*, vol. 38, no. 9, pp. 1444–1459, Sep. 2021.
[38] C. Mears, T. Lee, L. Ricciardulli, X. Wang, and F. Wentz, "Improving the accuracy of the cross-calibrated multi-platform (CCMP) ocean vector winds," *Remote Sens.*, vol. 14, no. 17, p. 4230, Aug. 2022.
[39] X. Wu et al., "Multi-task multi-objective evolutionary network for hyperspectral image classification and pansharpening," *Inf. Fusion*, vol. 108, Aug. 2024, Art. no. 102383.
[40] Z. Chen, G. Wu, H. Gao, Y. Ding, D. Hong, and B. Zhang, "Local aggregation and global attention network for hyperspectral image classification with spectral-induced aligned superpixel segmentation," *Expert Syst. Appl.*, vol. 232, Dec. 2023, Art. no. 120828.
[41] C. Cao, L. Bao, G. Gao, G. Liu, and X. Zhang, "A novel method for ocean wave spectra retrieval using deep learning from Sentinel-1 wave mode data," *IEEE Trans. Geosci. Remote Sens.*, vol. 62, 2024, Art. no. 4204016.
[42] X. Zhang, G. Gao, and S.-W. Chen, "Polarimetric autocorrelation matrix: A new tool for joint characterizing of target polarization and Doppler scattering mechanism," *IEEE Trans. Geosci. Remote Sens.*, vol. 62, 2024, Art. no. 5213522.
[43] D. Hong et al., "Cross-city matters: A multimodal remote sensing benchmark dataset for cross-city semantic segmentation using high-resolution domain adaptation networks," *Remote Sens. Environ.*, vol. 299, Dec. 2023, Art. no. 113856.
[44] Y. Ding et al., "Multi-scale receptive fields: Graph attention neural network for hyperspectral image classification," *Expert Syst. Appl.*, vol. 223, Aug. 2023, Art. no. 119858.
[45] D. Hong, J. Yao, C. Li, D. Meng, N. Yokoya, and J. Chanussot, "Decoupled-and-coupled networks: Self-supervised hyperspectral image super-resolution with subpixel fusion," *IEEE Trans. Geosci. Remote Sens.*, vol. 61, 2023, Art. no. 5527812.
[46] J. Feng et al., "Class-aligned and class-balancing generative domain adaptation for hyperspectral image classification," *IEEE Trans. Geosci. Remote Sens.*, vol. 62, 2024, Art. no. 5509617.
[47] D. Hong et al., "SpectralGPT: Spectral remote sensing foundation model," *IEEE Trans. Pattern Anal. Mach. Intell.*, vol. 46, no. 8, pp. 5227–5244, Aug. 2024.
[48] C. Li et al., "CasFormer: Cascaded transformers for fusion-aware computational hyperspectral imaging," *Inf. Fusion*, vol. 108, Aug. 2024, Art. no. 102408.
[49] H. Li, H. Wang, Y. Zhang, L. Li, and P. Ren, "Underwater image captioning: Challenges, models, and datasets," *ISPRS J. Photogramm. Remote Sens.*, vol. 220, pp. 440–453, Feb. 2025.
[50] H. Wang, K. Köser, and P. Ren, "Large foundation model empowered discriminative underwater image enhancement," *IEEE Trans. Geosci. Remote Sens.*, early access, Jan. 3, 2025, doi: 10.1109/TGRS.2025.3525962.
[51] Y. Xu et al., "Hyperspectral image super-resolution with ConvLSTM skip-connections," *IEEE Trans. Geosci. Remote Sens.*, vol. 62, 2024, Art. no. 5519016.
[52] H. Wang, W. Zhang, L. Bai, and P. Ren, "Metalantis: A comprehensive underwater image enhancement framework," *IEEE Trans. Geosci. Remote Sens.*, vol. 62, 2024, Art. no. 5618319.
[53] H. Wang, S. Sun, X. Bai, J. Wang, and P. Ren, "A reinforcement learning paradigm of configuring visual enhancement for object detection in underwater scenes," *IEEE J. Ocean. Eng.*, vol. 48, no. 2, pp. 443–461, Apr. 2023.
[54] H. Wang, W. Zhang, and P. Ren, "Self-organized underwater image enhancement," *ISPRS J. Photogramm. Remote Sens.*, vol. 215, pp. 1–14, Sep. 2024.
[55] H. Wang et al., "INSPIRATION: A reinforcement learning-based human visual perception-driven image enhancement paradigm for underwater scenes," *Eng. Appl. Artif. Intell.*, vol. 133, Jul. 2024, Art. no. 108411.
[56] Y. Li, W. Huang, X. Lyu, S. Liu, Z. Zhao, and P. Ren, "An adversarial learning approach to forecasted wind field correction with an application to oil spill drift prediction," *Int. J. Appl. Earth Observ. Geoinf.*, vol. 112, Aug. 2022, Art. no. 102924.
[57] Y. Li, X. Lyu, and P. Ren, "Oil spill timely backtracking oriented by wind field correction with self-attention temporal convolutional networks," *IEEE J. Ocean. Eng.*, vol. 49, no. 1, pp. 114–132, Jan. 2024.
[58] A. C. Toz and B. Koseoglu, "Trajectory prediction of oil spill with PISCES 2 around Bay of Izmir, Turkey," *Mar. Pollut. Bull.*, vol. 126, pp. 215–227, Jan. 2018.
[59] T. Nordam, C. Beegle-Krause, J. Skancke, R. Nepstad, and M. Reed, "Improving oil spill trajectory modelling in the Arctic," *Mar. Pollut. Bull.*, vol. 140, pp. 65–74, Mar. 2019.
[60] S. Xingjian, C. Zhourong, W. Hao, Y. Dit-Yan, W. Wai-Kin, and W. Wang-Chun, "Convolutional LSTM network: A machine learning approach for precipitation nowcasting," in *Proc. Adv. Neural Inf. Process. Syst. (NIPS)*, 2015, pp. 802–810.
[61] C. Lea, M. D. Flynn, R. Vidal, A. Reiter, and G. D. Hager, "Temporal convolutional networks for action segmentation and detection," in *Proc. IEEE Conf. Comput. Vis. Pattern Recognit. (CVPR)*, Jul. 2017, pp. 156–165.

Peng Ren (Senior Member, IEEE) received the B.Eng. and M.Eng. degrees in electronic engineering from Harbin Institute of Technology, Harbin, China, in 2003 and 2005, respectively, and the Ph.D. degree in computer science from the University of York, York, U.K., in 2010.

He is currently a Professor with the College of Oceanography and Space Informatics, China University of Petroleum (East China), Qingdao, China. His research interests include remote sensing and machine learning.

Dr. Ren was a recipient of the K. M. Scott Prize from the University of York in 2011 and the Eduardo Caianiello Best Student Paper Award at the 18th International Conference on Image Analysis and Processing in 2015, as one co-author.

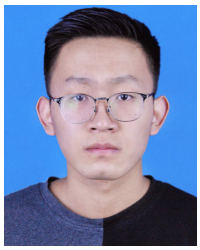

Qilin Jia received the B.Eng. degree in electronics and information engineering from China University of Petroleum (East China), Qingdao, China, in 2022, where he is currently pursuing the M.Eng. degree with the College of Oceanography and Space Informatics.

His research interests include analysis of marine disasters and machine learning with applications to remote sensing data.

Qing Xu received the B.Eng. degree from the School of Information and Electrical Engineering, Lu Dong University, Yantai, China, in 2023. She is currently pursuing the M.Eng. degree with the College of Oceanography and Space Informatics, China University of Petroleum (East China), Qingdao, China.

Her research interests include intelligent remote sensing and marine disasters.

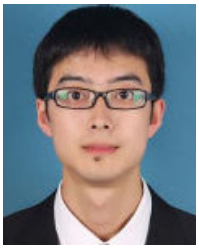

Yongqing Li received the B.Eng. degree in electronic information engineering, the M.Eng. degree in information and communication engineering, and the Ph.D. degree in control science and engineering from China University of Petroleum (East China), Qingdao, China, in 2013, 2016, and 2023, respectively.

He is currently a Lecturer with the School of Data Science, Qingdao University of Science and Technology, Qingdao. His research interests include oil spill detection, drift prediction, and backtracking.

Fan Bi received the B.Sc. degree in marine science and the Ph.D. degree in applied physical oceanography from the Ocean University of China, Qingdao, China, in 2008 and 2013, respectively.

She is a Senior Engineer at North China Sea Forecast and Hazard Mitigation Center, Ministry of Natural Resources, Qingdao. Her research interests include ocean wave modeling and ocean forecasting based on machine learning methods. She has made solid contributions to the projects including classification, fitting, and application of pacific swell dissipation rate based on ENVISAT data supported by the National Natural Science Foundation of China and maritime emergency disposal and decision-making, ocean forecasting system applications supported by the National Key Research and Development Program of China.

Jiangling Xu was born in Shandong, China, in 1982. She received the B.S. and M.S. degrees from the Ocean University of China, Shandong, in 2004 and 2007, respectively, and the Ph.D. degree from the University of Hamburg, Hamburg, Germany, in 2010.

Currently, she is a Professor Level Senior Engineer at North China Sea Forecast and Hazard Mitigation Center, Ministry of Natural Resources, Qingdao, China. Her research focuses on marine environmental numerical forecasting and data assimilation, as well as providing scientific support for emergency responses at sea.

Song Gao was born in Liaoning, China, in 1980. He received the B.S. and M.S. degrees from the Ocean University of China, Shandong, China, in 2004 and 2007, respectively.

He is a Professor Level Senior Engineer and the Deputy Director of North China Sea Forecast and Hazard Mitigation Center, Ministry of Natural Resources, Qingdao, China. His research is centered on marine environmental observation and forecasting, as well as marine disaster prevention and mitigation.